

AD-A159 540

A SEARCH FOR X-RAY CERENKOV RADIATION(U) NAVAL
POSTGRADUATE SCHOOL MONTEREY CA W R FRITCHIE JUN 85

1/1

UNCLASSIFIED

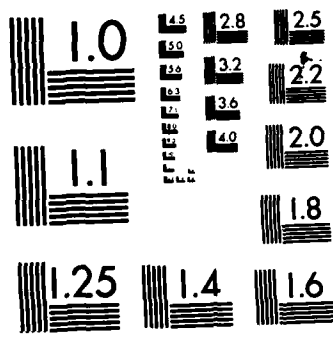
F/G 20/8

NL

END

FILMED

BYIC



MICROCOPY RESOLUTION TEST CHART
NATIONAL BUREAU OF STANDARDS-1963-A

AD-A159 540

NAVAL POSTGRADUATE SCHOOL
Monterey, California



DTIC
ELECTE
SEP 25 1985
S A D

THESIS

A SEARCH FOR X-RAY CERENKOV RADIATION

by

William Robert Fritchie

June 1985

Thesis Advisors:

J. R. Neighbours
X. K. Maruyama

DTIC FILE COPY

Approved for public release; distribution unlimited

85 9 24 064

UNCLASSIFIED

SECURITY CLASSIFICATION OF THIS PAGE (When Data Entered)

REPORT DOCUMENTATION PAGE		READ INSTRUCTIONS BEFORE COMPLETING FORM
1. REPORT NUMBER	2. GOVT ACCESSION NO. AD-A159540	3. RECIPIENT'S CATALOG NUMBER
4. TITLE (and Subtitle) A Search for X-ray Cerenkov Radiation		5. TYPE OF REPORT & PERIOD COVERED Master's Thesis; June 1985
		6. PERFORMING ORG. REPORT NUMBER
7. AUTHOR(s) William Robert Fritchie		8. CONTRACT OR GRANT NUMBER(s)
9. PERFORMING ORGANIZATION NAME AND ADDRESS Naval Postgraduate School Monterey, California 93943		10. PROGRAM ELEMENT, PROJECT, TASK AREA & WORK UNIT NUMBERS
11. CONTROLLING OFFICE NAME AND ADDRESS Naval Postgraduate School Monterey, California 93943		12. REPORT DATE June 1985
		13. NUMBER OF PAGES 57
14. MONITORING AGENCY NAME & ADDRESS (if different from Controlling Office)		15. SECURITY CLASS. (of this report) UNCLASSIFIED
		15a. DECLASSIFICATION/DOWNGRADING SCHEDULE
16. DISTRIBUTION STATEMENT (of this Report) Approved for public release; distribution unlimited		
17. DISTRIBUTION STATEMENT (of the abstract entered in Block 20, if different from Report)		
18. SUPPLEMENTARY NOTES		
19. KEY WORDS (Continue on reverse side if necessary and identify by block number) Cerenkov radiation x-ray index of refraction aluminum		
20. ABSTRACT (Continue on reverse side if necessary and identify by block number) Cerenkov x-ray emissions should not exist in media where the index of refraction is less than unity. In previous work, x-ray Cerenkov radiation at the K absorption edge of aluminum was reported to have been observed. The present experiment observed no x-ray Cerenkov radiation. However, radiation not characteristic of the Cerenkov mechanism was seen. The results of the experiment are provided. Various aspects of an experiment-		

DD FORM 1473

1 JAN 73

EDITION OF 1 NOV 65 IS OBSOLETE

S/N 0102-LF-014-6601

UNCLASSIFIED

SECURITY CLASSIFICATION OF THIS PAGE (When Data Entered)

UNCLASSIFIED

SECURITY CLASSIFICATION OF THIS PAGE (When Data Entered)

20. designed to investigate Cerenkov radiation in the x-ray region are also considered by exploring procedures, methods, equipment design and limitations. Suggestions for improvements to facilitate further experiments with media that allow the formation of Cerenkov radiation are provided. (Tesis.)

S N 0102- LF- 014- 6601

UNCLASSIFIED

SECURITY CLASSIFICATION OF THIS PAGE (When Data Entered)

Approved for public release; distribution unlimited

A Search for
X-ray Cerenkov Radiation

by

William R. Fritchie
Lieutenant, United States Navy
B.S., Marquette University, 1978

Submitted in partial fulfillment of the
requirements for the degree of

MASTER OF SCIENCE IN PHYSICS

from the

NAVAL POSTGRADUATE SCHOOL
June 1985

Author:

William R. Fritchie

William R. Fritchie

Approved by:

John R. Neighbours

John R. Neighbours, Co-Thesis Advisor

Xavier K. Maruyama

Xavier K. Maruyama, Co-Thesis Advisor

Gordon E. Schacher

Gordon E. Schacher, Chairman,
Department of Physics

John N. Dyer

John N. Dyer, Dean of Science and Engineering

ABSTRACT

Cerenkov x-ray emissions should not exist in media where the index of refraction is less than unity. In previous work, x-ray Cerenkov radiation at the K absorption edge of aluminum was reported to have been observed. The present experiment observed no x-ray Cerenkov radiation. However, radiation not characteristic of the Cerenkov mechanism was seen. The results of the experiment are provided. Various aspects of an experiment designed to investigate Cerenkov radiation in the x-ray region are also considered by exploring procedures, methods, equipment design and limitations. Suggestions for improvements to facilitate further experiments with media that allow the formation of Cerenkov radiation are provided.

TABLE OF CONTENTS

I.	INTRODUCTION	10
II.	THEORY	12
	A. CHARACTERISTICS OF X-RAY CERENKOV RADIATION	12
	B. DETERMINATION OF THE INDEX OF REFRACTION IN THE X-RAY REGION	15
III.	THE EXPERIMENT	19
	A. THE EQUIPMENT	19
	1. The Test Chamber	19
	2. The Internal Detection Apparatus	19
	3. The Gas Flow System	22
	4. The External Detection Apparatus	23
	5. The Linear Accelerator	27
	B. TEST CHAMBER GEOMETRY	29
	C. EXPERIMENTAL CONSIDERATIONS	30
	1. Calibrating the Equipment	30
	2. The Noise Problem	33
	3. Argon Gas Contamination	34
IV.	RESULTS AND DISCUSSION	37
	APPENDIX A. LIST OF EQUIPMENT	47
	APPENDIX B. GENERAL PROCEDURES	48
	A. PLACING THE SYSTEM UNDER VACUUM	48
	B. PRESSURIZING THE PROPORTIONAL COUNTER	49
	C. VENTING THE SYSTEM	50

APPENDIX C. MANUFACTURING THIN WINDOWS	-----	51
APPENDIX D. MEASUREMENTS AND CALCULATIONS	-----	53
LIST OF REFERENCES	-----	56
INITIAL DISTRIBUTION LIST	-----	57

LIST OF TABLES

I.	Optical Properties of Aluminum -----	18
II.	The Limits of Movement of the Proportional Counter -----	30
B-I.	Valve Alignment for Placing System under Vacuum --	49
C-I.	Procedure for the Manufacture of Thin Windows ----	52

LIST OF FIGURES

2.1	Cerenkov Radiation Pattern	13
2.2	Atomic Scattering Factor of Aluminum	16
3.1	The Target and Test/Detector Chambers	20
3.2	The Proportional Counter	21
3.3	The Gas Flow System	23
3.4	The NPS Linear Accelerator	24
3.5	X-ray Photon Counting Apparatus	25
3.6	Electron Beam Monitoring Apparatus	27
3.7	Camera Placement in the End Station	28
3.8	PHA Display at 210 Torr	31
3.9	PHA Display at 260 Torr	32
3.10	PHA Display at 310 Torr	32
3.11	Pumping Speed at Various Pressures - Air	36
3.12	Pumping Speed at Various Pressures - Noble Gases	36
4.1	PHA Display of Background Radiation	38
4.2	PHA Display of Background Radiation after 2 hours	38
4.3	PHA Display Showing Klystron Noise	40
4.4	PHA Display at 250 Turns (2.382°)	41
4.5	PHA Display at 260 Turns (2.105°)	41
4.6	PHA Display at 270 Turns (1.828°)	42
4.7	PHA Display at 275 Turns (1.690°)	42
4.8	Graph of Experimental Results	44
4.9	Graph of Comparison with [Ref. 4]	45
D.1	Test Chamber Dimensions	54

ACKNOWLEDGEMENT

My thanks to:

Don Snyder, for his long hours in the lab.

My wife, Rose Anne, for her long hours in front of the
Apple IIe.

I. INTRODUCTION

Cerenkov radiation results when a charged particle or group of charged particles exceeds the speed of light in a medium. This phenomenon was first investigated by Cerenkov in 1934 and, until recently, subsequent investigations have been restricted almost entirely to radiation in the optical region. These concentrated efforts in the optical region were due to the widespread belief that Cerenkov radiation was not possible at other frequencies [Ref. 1].

The velocity of light in a given medium is described as:

$$c = c_0/n \quad (1.1)$$

where c_0 is the velocity of light in a vacuum, and n is the index of refraction of the given medium. Since the index of refraction of all media is generally less than unity over the entire x-ray region, Cerenkov radiation at x-ray frequencies would not be possible.

Recently, however, Bazylev et al. [Ref. 2] theorized that near the photoabsorption edges, the coupling of the relativistic electrons with the atoms of the given medium alters the index of refraction of that medium, resulting in small areas in the x-ray region where the real part of the index of refraction is greater than unity. The experiment stemming from this theory obtained Cerenkov

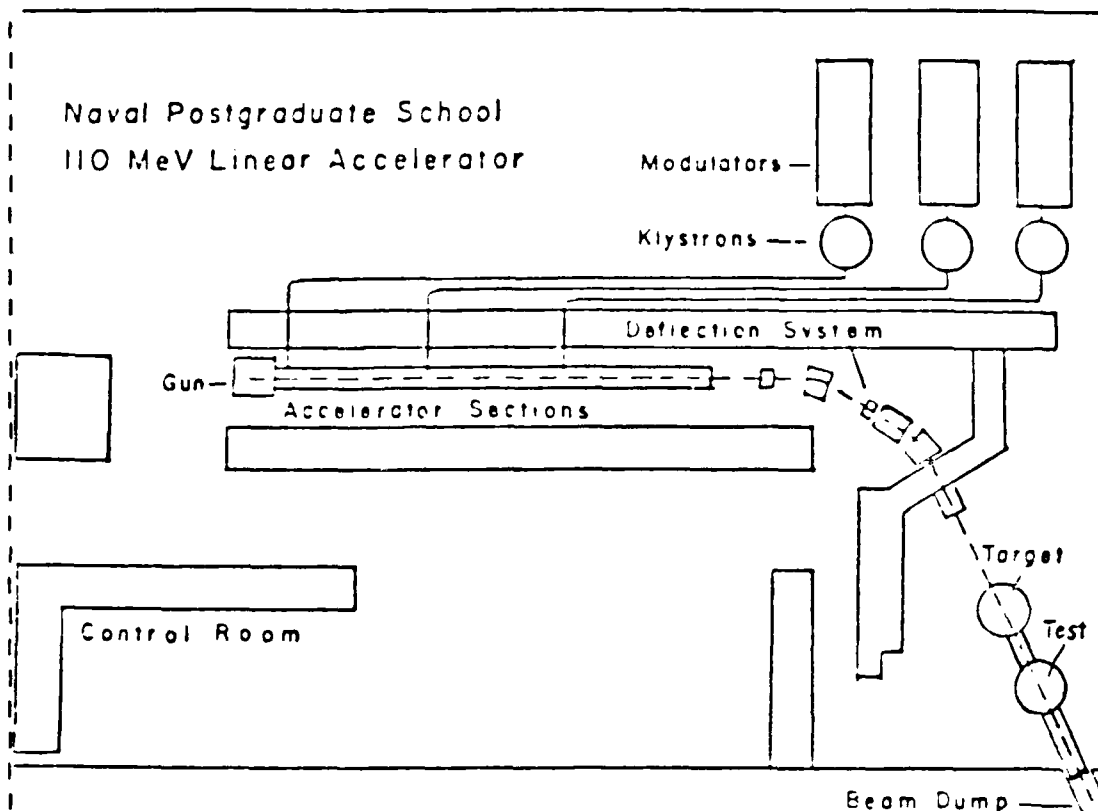


Figure 3.4 The NPS Linear Accelerator.

amplification. The amplified signal, now strong enough to be measured, is sent to an oscilloscope for visual observation, and is also accumulated for display on the Pulse Height Analyzer (PHA). The PHA allows the detection range to be divided up into channels, and the signal counts are recorded on a two dimensional plot. The resulting display is a pulse height distribution, and the pulse heights are proportional to the incident photon energies, making the display essentially an energy spectrum.

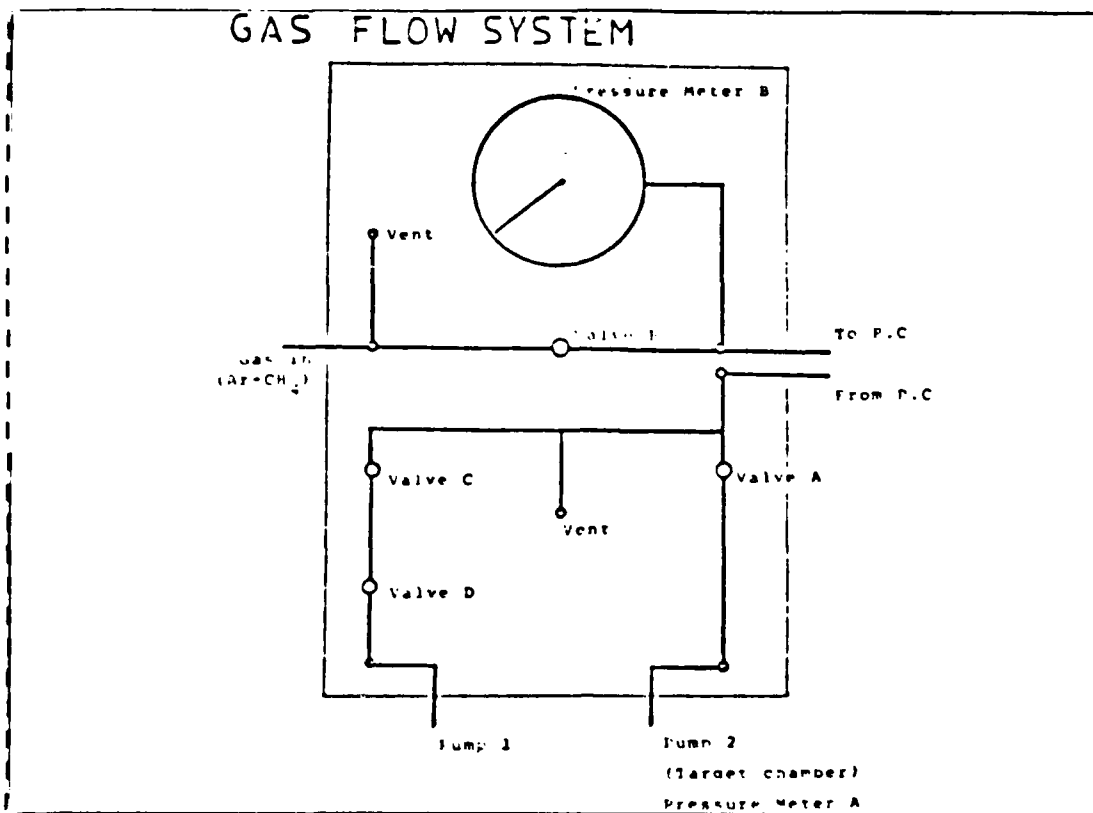


Figure 3.3 The Gas Flow System.

4. The External Detection Apparatus

The external apparatus for this experiment is kept in the end station, or target area, and in the control room, whose location is shown in Figure 3.4.

The apparatus used for counting the x-ray photons is shown in a block diagram in Figure 3.5. The proportional counter, receiving bias voltage from a d.c. power supply, is connected to a preamplifier, also powered by the d.c. power supply. The signal received from the proportional counter is shaped by the preamplifier and sent to the amplifier for

chamber regardless of the position of the proportional counter along the axis of movement.

3. The Gas Flow System

The gas flow system is designed to serve a twofold purpose. The system will enable the proportional counter to be placed under the same high vacuum as the test chamber, or it can be used to pressurize the proportional counter with a gas mixture above the high vacuum of the test chamber. The gas mixture, as described above, will reduce the number of electron-ion pairs generated by the low energy photons.

There were two mixtures of gases that were used in working with the low energy photons. The mixture of 90% argon, 10% methane, or P-10 gas, will allow an adequate number of electron-ion pairs to be generated to give a good display over most of the energy spectrum on the Pulse Height Analyzer (PHA). A mixture with a greater percentage of hydrocarbons, however, such as a 50% argon, 50% methane (P-50) gas, will enhance the energy spectrum display on the PHA for energies below 1.5 KeV.

The procedures for placing the proportional counter under vacuum, pressurizing it, and bringing the system up to atmosphere is discussed in Appendix B. The gas flow system is shown in Figure 3.3.

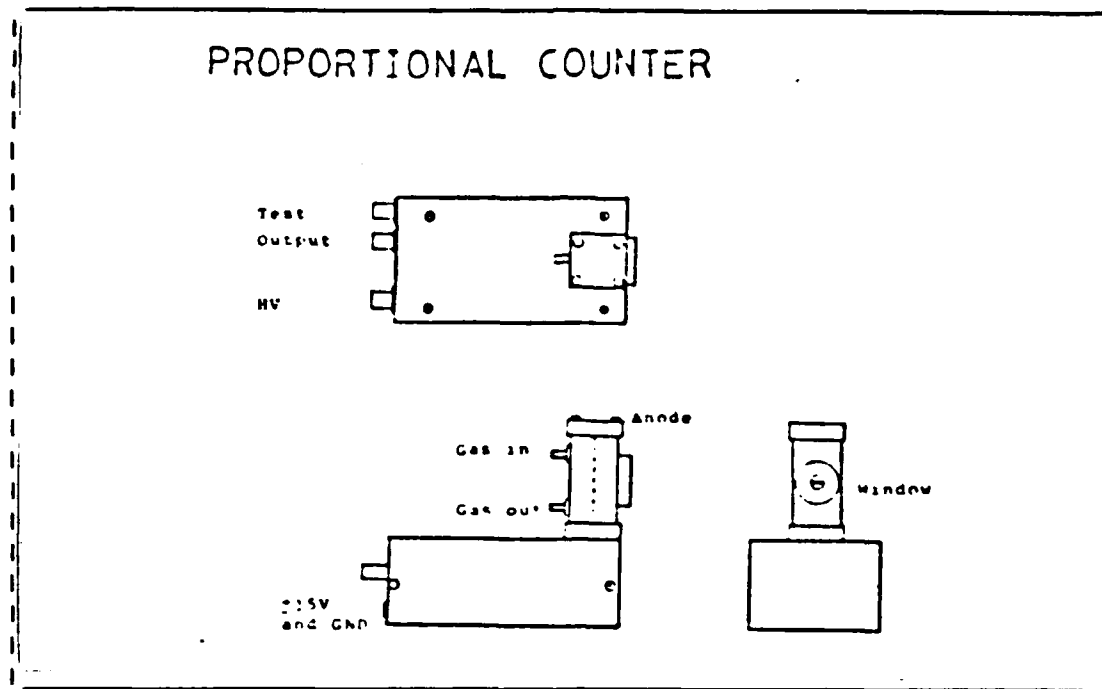


Figure 3.2 The Proportional Counter.

proportional counter is protected against high voltage breakdown, a phenomenon that occurs when the vacuum is not high enough.

During this experiment, the proportional counter was pressurized with a gas mixture via the gas flow system in order to reduce the number of electron-ion pairs generated by the low energy photons and enabling the resultant pulses to cover a broad signal range. The proportional counter can be raised and lowered on a vertical axis by a small motor mounted external to the test chamber, as shown in Figure 3.1. The window will always face the target in the target

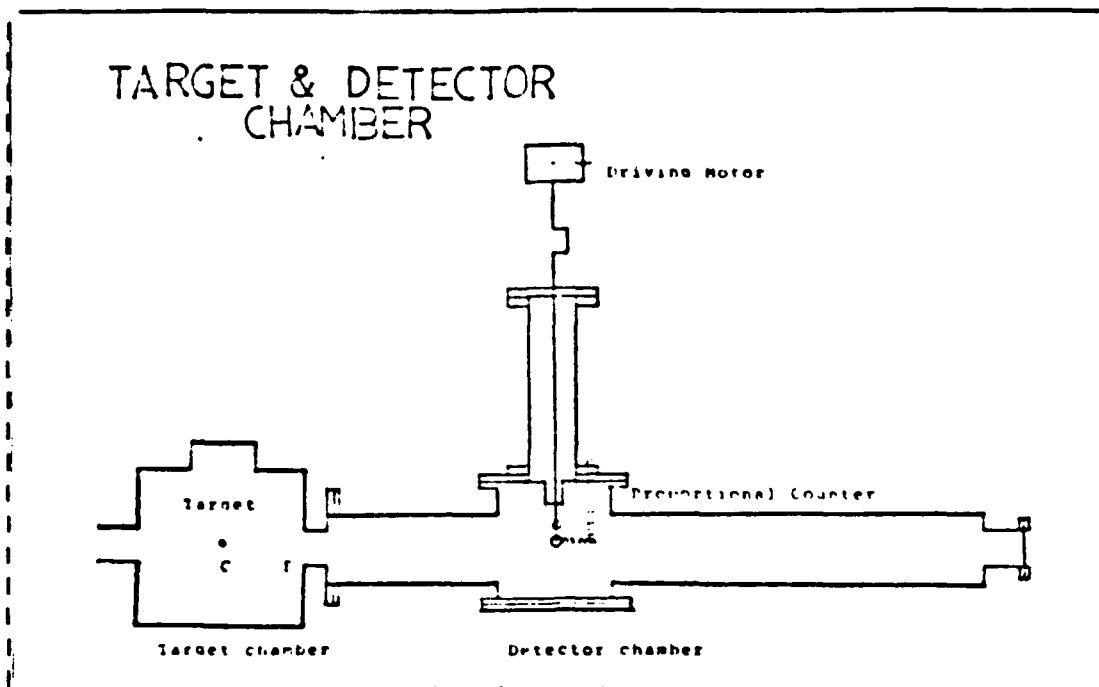


Figure 3.1 The Target and Test/Detector Chambers.

slot, and has an operating differential pressure of about 400 Torr, with a maximum differential pressure of 800 Torr [Ref. 7].

In the experimental setup proposed by Choi [Ref. 6], a pulse amplifier was attached to the proportional counter, as shown in Figure 3.2. The pulse amplifier subsequently failed and was removed [Ref. 6], but the container holding the pulse amplifier remained in place. A new proportional counter preamplifier was installed external to the test chamber. The new preamplifier is a charge sensitive unit that is designed for use with proportional counters in applications such as this experiment. This

III. THE EXPERIMENT

A. THE EQUIPMENT

Specific equipment used in this experiment is listed in Appendix A.

1. The Test Chamber

The test chamber to be used in this experiment is constructed of aluminum, and is the same chamber used by Farmer [Ref. 4] and Choi [Ref. 6]. Figure 3.1 shows both the target and the test/detector chambers. The test chamber is bolted to the target chamber and is at the same vacuum pressure. Typically, vacuum of the order of 10^{-5} Torr was obtained under experimental conditions.

2. The Internal Detection Apparatus

The detection apparatus for the x-ray is a gas flow proportional counter (photon counter), shown in Figure 3.2. The cathode is composed of nickel plated brass, cylindrical symmetry, an inner dimension of 1.95 cm and an overall length of 7.3 cm. The anode is 50 microns in diameter, and composed of nichrome or stainless steel. The thin window of the counter is made up of VYNS, a combination of vinyl acetate and vinyl chloride, with a thickness of approximately 1000 angstroms, and a 58% transmission 400 mesh screen for support. The VYNS window covers a 3x10 mm

TABLE I
Optical Properties of Aluminum

<u>Absorption Edges</u>	<u>Energy in eV</u>	<u>Real Part (n)</u>	<u>Imaginary Part (k)</u>
L1	86	1.0059	0.028233
	87	1.0055	0.028496
	88	1.0054	0.028958
L2,3	72.6	1.03	0.00395
	72.7	1.0339	0.012328
	72.8	1.0302	0.019984
K	1558	0.99992	0.000029
	1559	0.99992	0.000033
	1560	0.99992	0.000041

D. V. Smith et al. [Ref. 5] and the results are tabulated in Table I. It should be noted that the index of refraction for the K edge of aluminum is less than unity, and therefore fails to meet the requirement for the formation of Cerenkov radiation. It is for this reason that Farmer's experiment [Ref. 4] needs to be repeated. This experiment will duplicate the conditions set by Farmer [Ref. 4], but due to equipment limitations to be discussed in the next section, the soft x-rays of the L1 and L2,3 edges of aluminum will not be looked at.

Although practically all of the x-ray region falls into the above category of positive values of f_1 in determining the index of refraction, a closer look at the dielectric constant at the absorption edges leads to negative values of f_1 and corresponding indices of refraction greater than unity. The dielectric constant of the given medium, K , related to the index of refraction by Equation 2.1, and f_1 and f_2 by Equations 2.9 and 2.10, is both complex and a function of ω and can be written as:

$$K(\omega) = K_r(\omega) + iK_i(\omega) \quad (2.11)$$

where $K_r(\omega)$ and $K_i(\omega)$ are the real and imaginary parts of the dielectric constant. The above relation stems from the Kramers-Kronig dispersion relation:

$$K_r(\omega) - 1 = \frac{2}{\pi} \int_0^{\infty} (\omega' K_i(\omega') / (\omega'^2 - \omega^2)) d\omega' \quad (2.12)$$

This relation was used to find the index of refraction for x-rays from measured absorption. The main point of this relation is that K_i , a measure of absorption, has a corresponding measure of dispersion, K_r . If $K_i(\omega)$ is known for a particular range of frequencies, then $K_r(\omega)$ can be determined using the above relation.

Redefining the real and imaginary part of the index of refraction in terms of K_r and K_i :

$$n = [1/2 (K_r + \sqrt{K_r^2 + K_i^2})]^{1/2} \quad (2.13)$$

$$k = [1/2 (-K_r + \sqrt{K_r^2 + K_i^2})]^{1/2} \quad (2.14)$$

Values of n and k , in terms of K_r and K_i , for the case of aluminum at the absorption edges has been calculated by

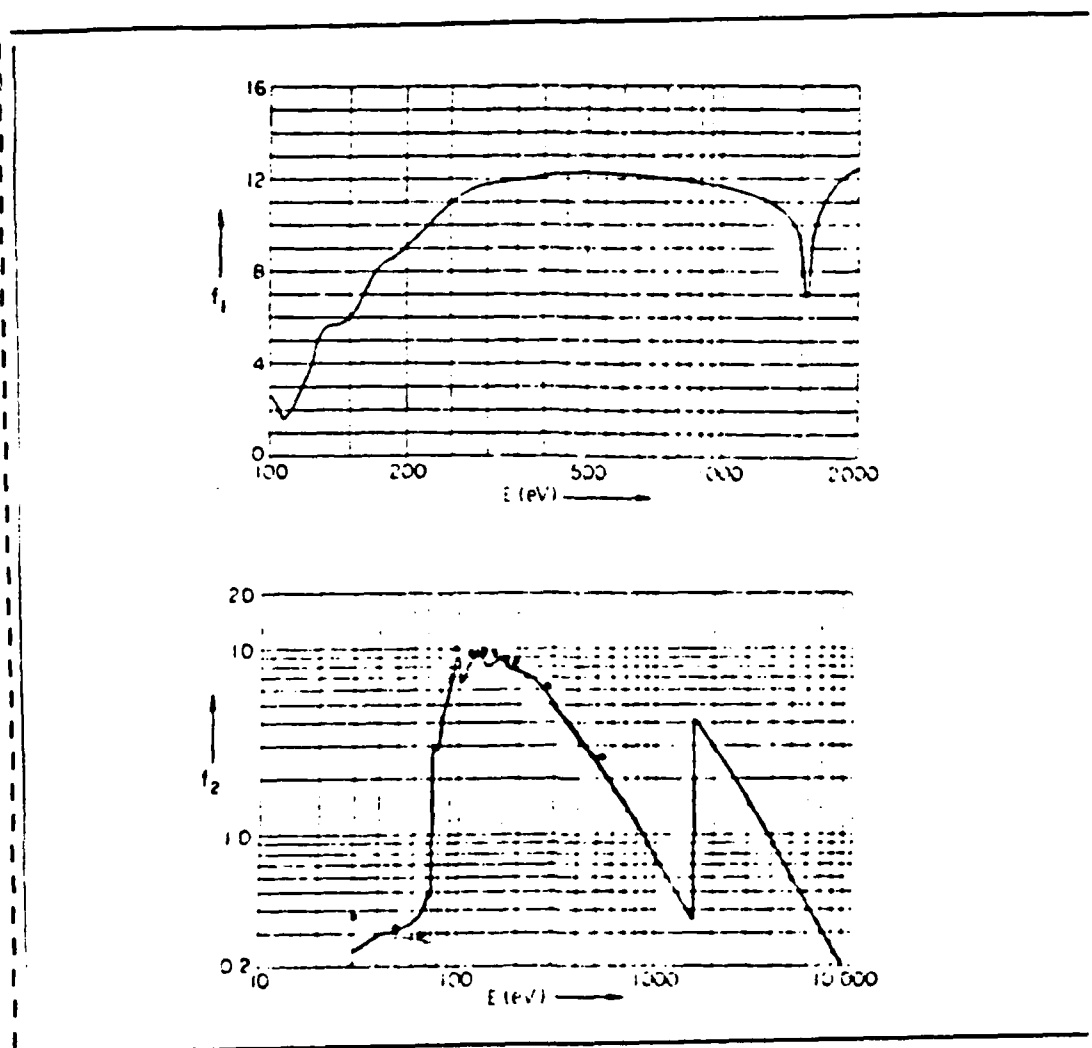


Figure 2.2 Atomic Scattering Factor of Aluminum.

the real part of the index of refraction, to be greater than unity in this region, f_1 has to be negative. Typical values of f_1 as well as f_2 are tabulated by Henke et al. [Ref. 3]. The region where f_1 is negative is extremely small, as shown in Figure 2.2 at 1.56 KeV for the case of aluminum, and apparently not well calculated.

B. DETERMINATION OF THE INDEX OF REFRACTION IN THE X-RAY REGION

The atoms that make up a given medium can be treated classically as an oscillator consisting of an electron of mass m_e vibrating about a more massive positive charge [Ref. 1]. When these oscillators are excited by an electromagnetic wave having angular frequency ω the resultant motion of the electron can be described as:

$$d^2x + kdx + \omega_s^2 x = (e E_0 / m_e) \exp(i\omega t) \quad (2.6)$$

where k is the damping factor, and ω_s is the natural frequency of the dipole neglecting external forces, and E_0 is the complex electric field amplitude.

The scattering factor of the dipole, f , defined as the ratio of the oscillator scattered amplitude to the free classical electron scattered amplitude, can be written as:

$$f = \omega^2 / (\omega_s^2 - \omega^2 + i k \omega) \quad (2.7)$$

The scattering factor is made up of a real and an imaginary part, written as:

$$f = f_1 + i f_2 \quad (2.8)$$

These variables can be used to describe the real and imaginary parts of the index of refraction in the x-ray region, n and k , respectively:

$$n = 1 - (N e^2) / (\epsilon_0 m_e \omega^2) f_1 \quad (2.9)$$

$$k = (N e^2) / (\epsilon_0 m_e \omega^2) f_2 \quad (2.10)$$

where m_e is the electron mass, e the electron charge, ϵ_0 the permittivity of free space, and N the atom density. For n ,

well as the dielectric constant K , by the following equation:

$$n = \sqrt{\epsilon/\epsilon_0} = \sqrt{K} \quad (2.1)$$

The time it takes light to travel the distance AB , then, can be written as:

$$AB = ct = (c_0/n)t \quad (2.2)$$

The speed of the charged particle in the medium is defined as:

$$v = \beta c_0 \quad (2.3)$$

where β is defined as v/c_0 . The time it takes the charged particle to travel the distance AC can be written as:

$$AC = vt = \beta c_0 t \quad (2.4)$$

From the above, the Cerenkov relation can be stated as follows:

$$\cos \theta_c = AB/AC = 1/n\beta \quad (2.5)$$

X-ray Cerenkov radiation will only occur if the index of refraction of the given medium is greater than unity. This condition applies only at the absorption edges. The index of refraction at the absorption edges is quite small, necessitating relativistic velocities for the charged particles, and resulting in extremely small radiation angles. The theory used to describe dispersionless Cerenkov radiation in the optical region, therefore, must be extended to include the frequency dependence of the index of refraction.

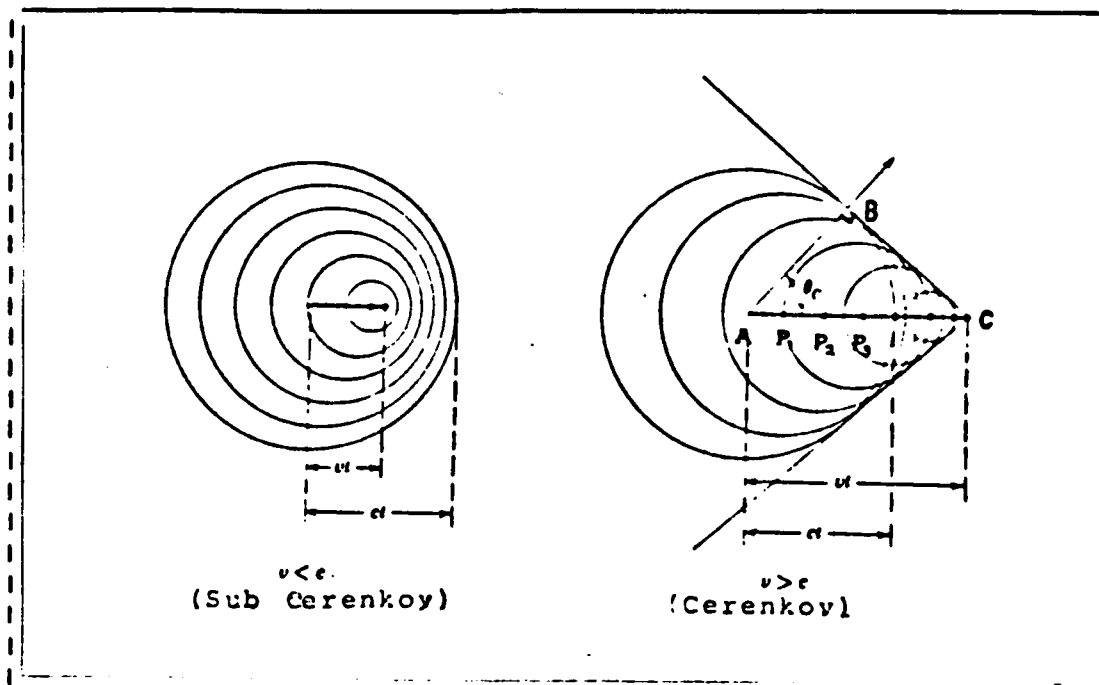


Figure 2.1 Cerenkov Radiation Pattern.

of points along the path of the charged particle are coherent and form a wave front. The coherence occurs when the charged particle travels a distance AC in the same amount of time as it takes light to travel the distance AB. The speed of light in the medium is defined in Equation 1.1 as:

$$c = c_0/n \quad (1.1)$$

where c_0 is the speed of light in a vacuum and n is the index of refraction. Here, n is related to the permittivity of the medium, ϵ , and the permittivity of free space, ϵ_0 , as

II. THEORY

A. CHARACTERISTICS OF X-RAY CERENKOV RADIATION

A charged particle moving at a velocity close to the speed of light in a given medium, provided that the permittivity of the medium is greater than the permittivity of free space, will generate a dipole field. The field generated at each element in the medium is temporary, as each element will then radiate an electromagnetic pulse. The resultant radiation will cover a broad band of frequencies corresponding to the various Fourier components of the pulse. [Ref. 1]

The radiation generated by these elements along the path of the charged particle are often described as tiny wavelets. These wavelets normally disappear due to destructive interference, and the far field intensity will remain at zero. If the velocity of the charged particle is greater than the phase velocity of the light in the given medium, however, the wavelets may be in phase with each other, and the far field intensity will not be zero. [Ref. 1]

If the above condition is met, radiation will be observed, but only at a certain angle with respect to the path of the charged particle. As shown in Figure 2.1, this angle, θ_c , is the angle at which the wavelets from any set

radiation from carbon at a wavelength of 40 angstroms.
[Ref. 2]

Henke et al. calculated the index of refraction to be less than unity for the K edge of aluminum [Ref. 3]. In variance with these calculations, W. J. Farmer [Ref. 4] reported a measurement of Cerenkov radiation in the x-ray region at the K edge of aluminum. This experiment shows that the results of Farmer's experiment [Ref. 4] are probably due to sources other than Cerenkov radiation.

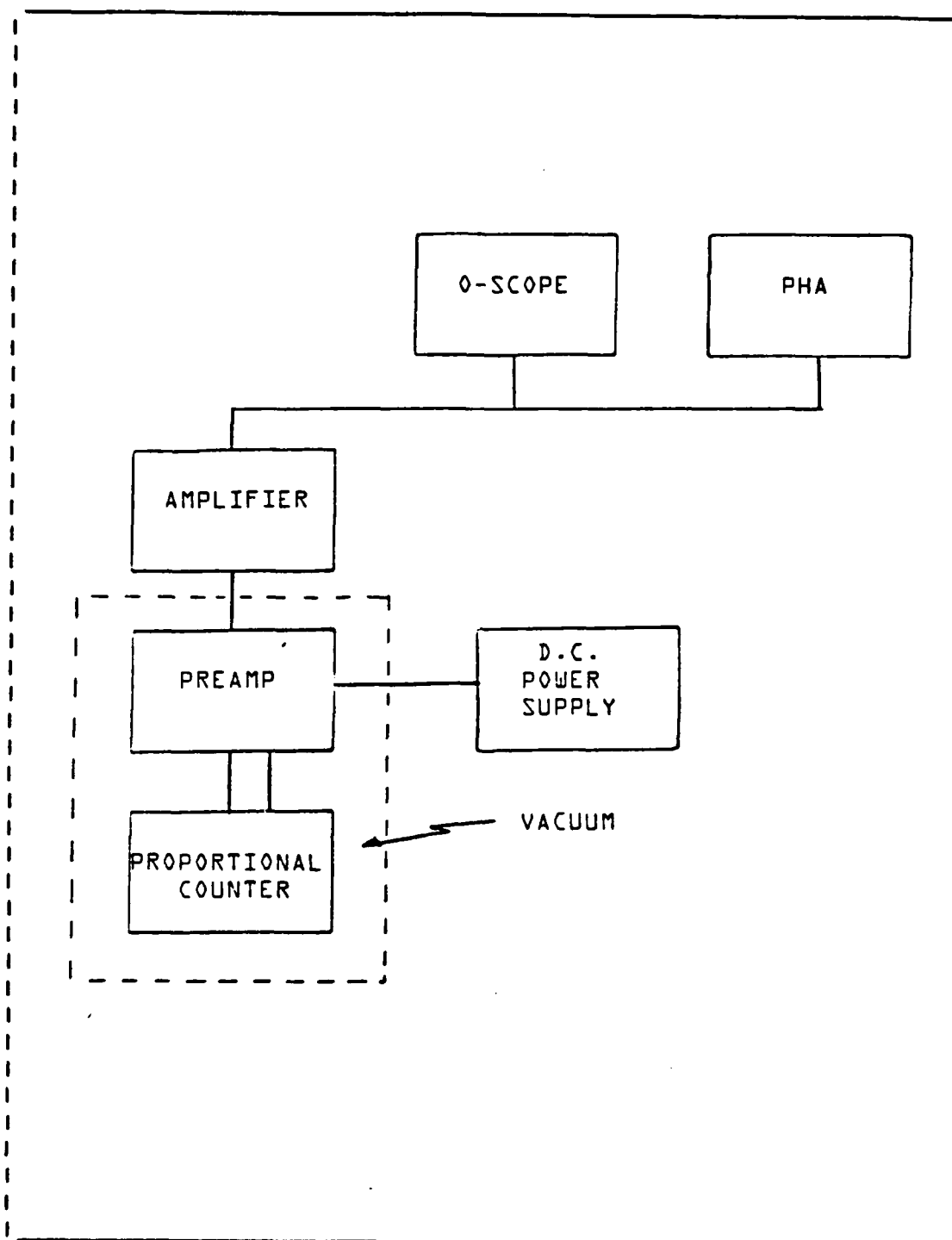


Figure 3.5 X-ray Photon Counting Apparatus.

The apparatus used to monitor the electron beam is shown in a block diagram in Figure 3.6. A plastic scyntillation crystal masked in black tape is attached to a photomultiplier tube and positioned at the exit point of the test chamber. The photomultiplier tube receives its bias voltage from a d.c. power supply. The photons striking the crystal are reproduced as electronic signals by the photomultiplier tube and are registered on one of the digital counters. A lead from the linear accelerator machine trigger to the other digital counter allows the monitoring of the number of machine pulses.

The apparatus used to control the movement of the proportional counter in the test chamber is a remote control device. It consists of a vernier dial for motor voltage, an on-off switch, and a directional control. The remote control device is located in the control room.

In order to visually monitor the equipaent in the end station area, several television cameras were positioned in the end station as shown in Figure 3.7. The television monitors, located in the control room, allow the operator to monitor the vacuum, the gas flow system, the beam dump area, the turn counter on the motor controlling the position of the proportional counter, and the target area inside the target chamber via a glass port on the side of the target chamber.

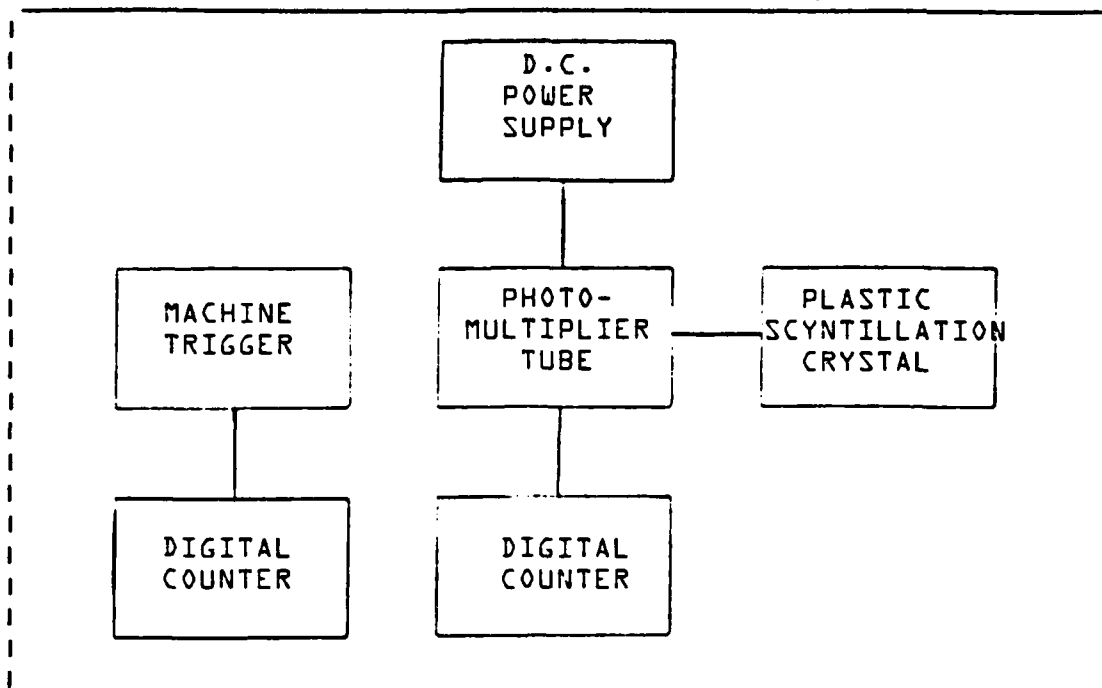


Figure 3.6 Electron Beam Monitoring Apparatus.

5. The Linear Accelerator

The Naval Postgraduate School's linear accelerator, or linac, shown in Figure 3.4, produces a beam consisting of electron bunches, and has the following operating characteristics: 120 MeV maximum energy, 3-5 μ Amp maximum average current, 2.856 GHz operating frequency, and a 1.0 μ sec pulse duration. An electron gun at the head of the accelerator injects electrons of 80 KeV into the beam pipe. Three klystron tubes provide RF power to the three individual accelerator sections, and the injected electrons are quickly accelerated to velocities near the speed of light within the first few centimeters of travel. The beam,

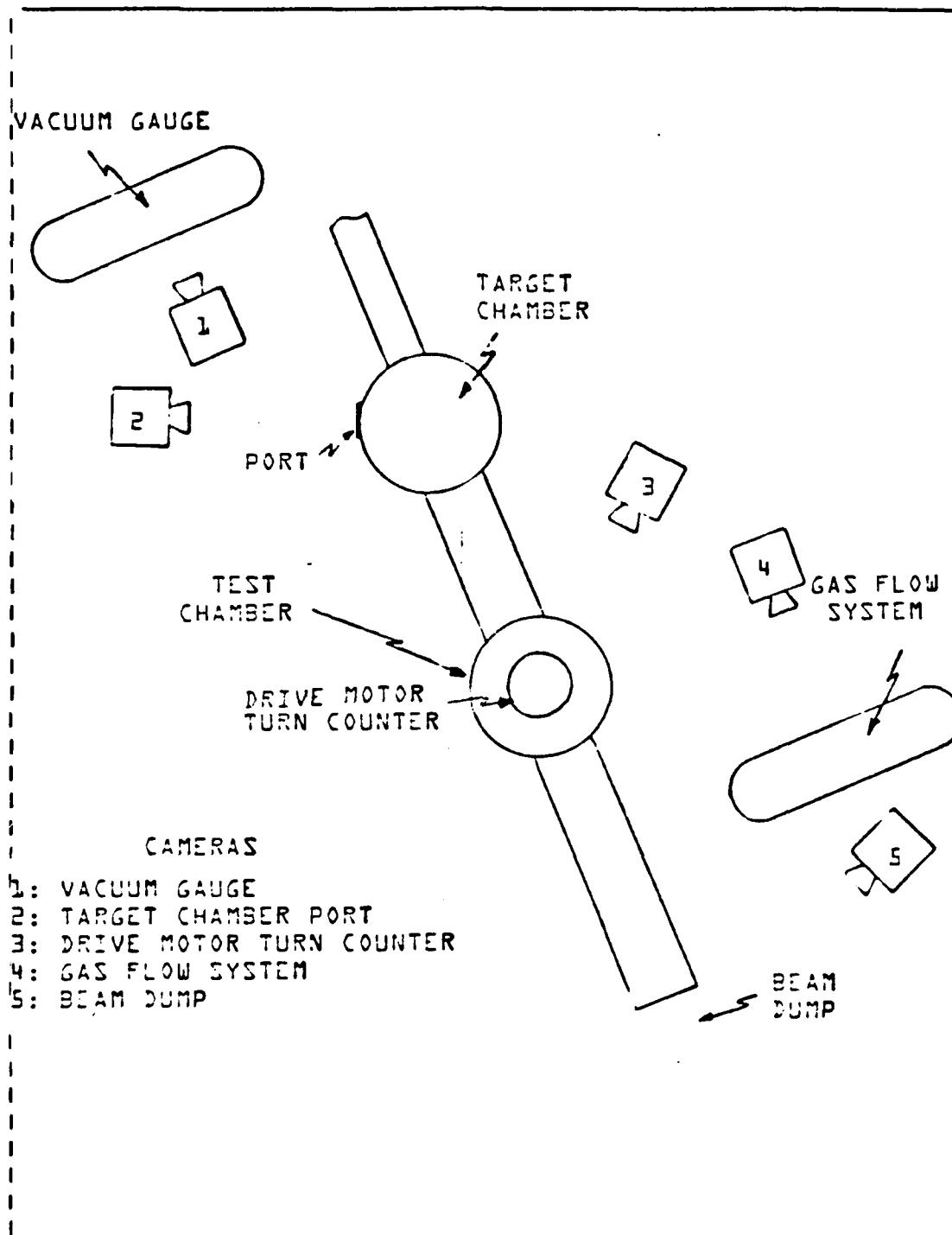


Figure 3.7 Camera Placement in the End Station.

composed of these electron bunches, is then bent by a magnet, thereby separating the high energy electrons. A tungsten slit further separates the desired high energy electrons, and a set of steering and quadrupole magnets focus the resultant beam on the target in the target chamber. The beam then passes through the target chamber, as well as the test chamber, and into the beam dump. In the present experiment, extremely low currents were required, so the electron gun was not turned on. The source of electrons was the "dark current" of stray electrons accelerated by the linac.

B. TEST CHAMBER GEOMETRY

The proportional counter movement on a vertical axis within the test chamber results in an angular displacement off the beam axis. The upper and lower limits of vertical movement, the corresponding angular displacement as well as the turn count reading on the proportional counter drive motor are listed in Table II. From this table it can be concluded that the present apparatus will allow the detection of Cerenkov radiation of the Cerenkov angle as greater than 1.313° and less than 6.537° .

Cerenkov radiation for the K edge of aluminum reported by Farmer [Ref. 4] for a target of thickness $25.4 \times 10^{-5} \text{ m}$, or 1 mil, was at 32 mrad, or 1.824° . This is within the limits of the vertical movement of the proportional counter.

TABLE II

The Limits of Movement of the Proportional Counter

	Minimum	Maximum
Distance	1.82 cm	7.5 cm
Turns	278	100
Angle	1.313°	6.537°

A more detailed analysis of the geometry of the test chamber is given in Appendix D.

C. EXPERIMENTAL CONSIDERATIONS

1. Calibrating the Equipment

Prior to running the actual experiment, calibrating the equipment with a low energy source is required in order to make sense out of future experimental data. The low energy source used in preparation for the experiment was Fe^{55} . The source was placed in the test chamber at the same height as the thin window of the proportional counter, and the entire apparatus was placed under vacuum. A P-10 gas mixture was introduced via the gas flow system. Figure 3.8 shows a typical PHA display that indicates the Fe^{55} peak at 5.89 KeV, which in turn, excites the K edge of Argon at 3.19 KeV. Comparing the channel numbers of the peaks and the zero channel of the PHA demonstrates a linear relationship.

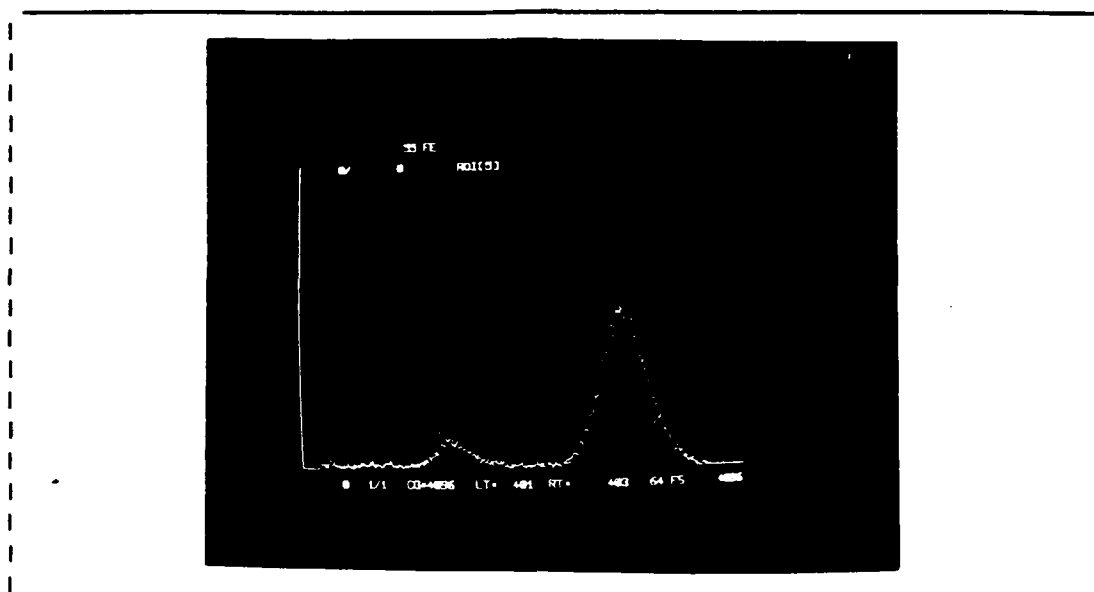


Figure 3.8 PHA Display at 210 Torr.

While conducting the preliminary benchwork, it was noted that the proportional counter was extremely sensitive to changes in pressure and voltage. As an example of the pressure sensitivity Figures 3.9 and 3.10 show a PHA display under the same conditions as in Figure 3.8, with the exception of the gas pressure. Figure 3.8 is a result of a gas pressure of 210 Torr, Figure 3.9 at 260 Torr, and Figure 3.10 at 310 Torr. The increase in gas pressure moves the entire display to the left as well as severely restricting the resolution of the display.

The voltage sensitivity involves an increase in the amount of counts per channel as the voltage is increased, thereby enhancing the energy spectrum display on the PHA. After careful examination a pressure of 200 Torr and a high

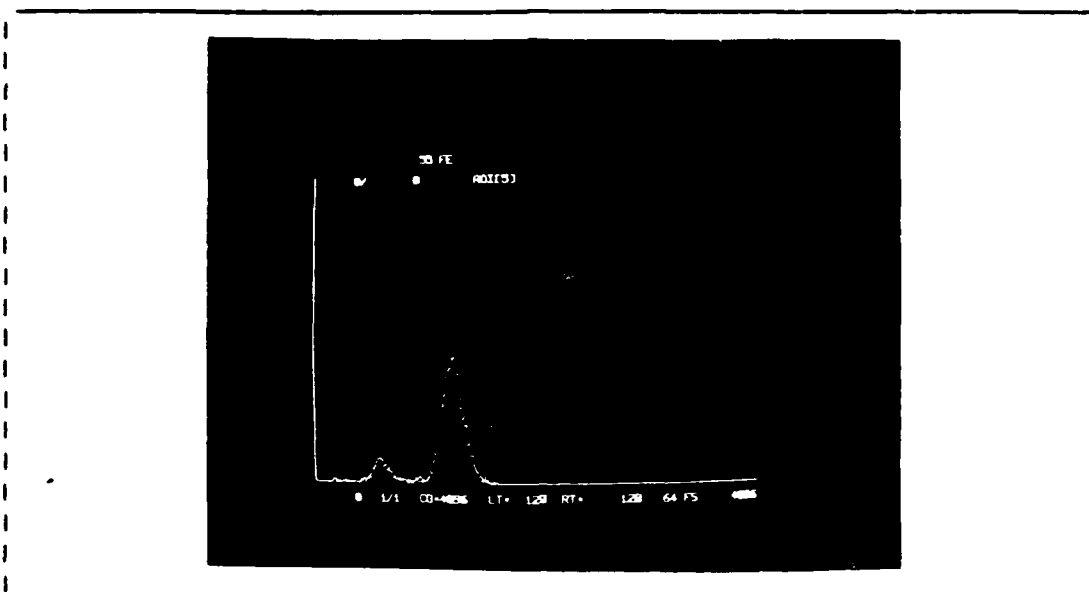


Figure 3.9 PHA Display at 260 Torr.

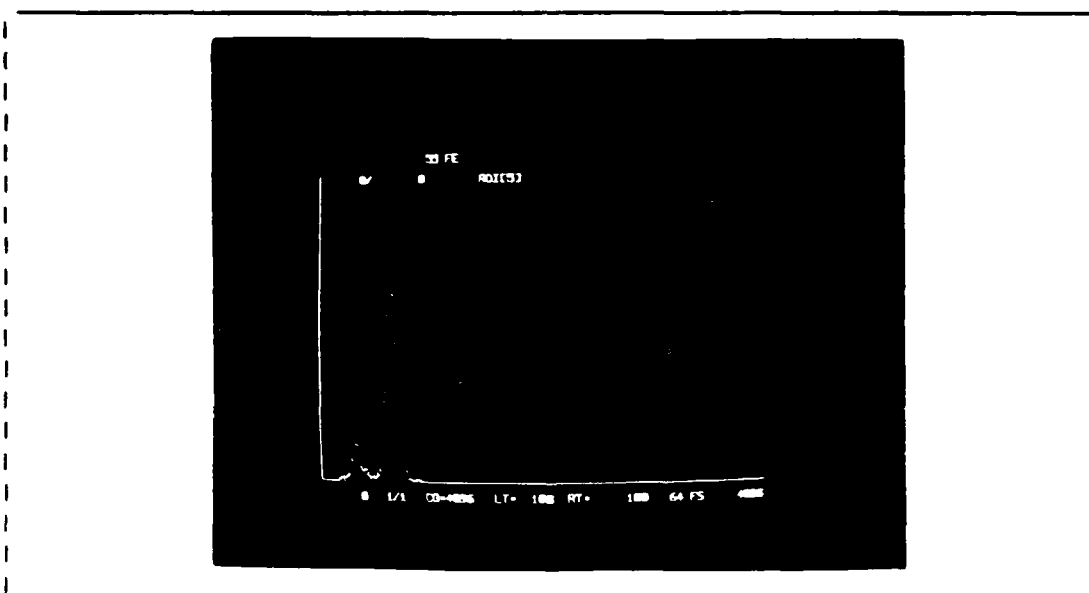


Figure 3.10 PHA Display at 310 Torr.

voltage setting of 900 V provided the best resolution on the PHA display for the P-10 gas. Subsequent treatment of the P-50 gas led to a pressure of 200 Torr and a high voltage setting of 1100 V for best resolution. Based on these displays, the equivalent channels per Torr was calculated to be 23.7 channel/Torr. At best resolution of 1.05 KeV (full width half max.), the equivalent electron volts per channel was calculated to be 1.95 eV/ channel.

2. The Noise Problem

The lower level discriminator (LLD) control on the PHA was used to cut out the lower channels, as they were filled with random noise from the equipment. The random noise covered a significant range in the lower end of the energy spectrum, which would mask lower energy peaks such as the K edge of carbon at 0.28 KeV. The installation of the preamplifier into the aluminum container that once housed the pulse amplifier for Choi's experiment [Ref. 6] proved to be the necessary modification. The noise level was reduced to near zero, measured on the most sensitive scales of the PHA.

Investigating the noise problem involved experimenting with various grounding and shielding techniques. The cable from the preamplifier to the test chamber, approximately five inches in length, caused noise at a rate of 800 counts per second. Placing grounding straps over and around the cable reduced the noise level by a factor of ten.

Tightening the ends of the grounding strap with base clamps on the ends of the cable reduced the noise factor again, this time by a factor of two. Grounding the cable and grounding strap with alligator clips also reduced the noise level by a factor of two.

In summary, the grounding and shielding reduced the low noise, but there were too many floating grounds. It was noted that the slightest movement of the preamplifier and/or the cable either created more noise or shifted the spectrum. It was also noted that the alligator clips sometimes acted as antennae, further revealing the sensitivity of the apparatus. The installation of the preamplifier into the vacuum chamber eliminated the electronic noise sources.

3. Argon Gas Contamination

Upon opening the end gate valve of the linear accelerator, the beam pipe, as well as the test chamber and target chamber become one vacuum system. As a rule, the test chamber and target chamber are usually an order of magnitude lower in vacuum than the linear accelerator itself. The linear accelerator ion pumps can usually handle the extra load if the gas mixture is of a normal atmospheric content.

Due to a small leak in the high voltage connection of the proportional counter, however, which was later located and repaired, a P-50 gas mixture leaked into the test chamber and target chamber as well as the accelerator

beam pipe. This gas mixture had an adverse effect on the ion pumps.

The basic principle of an ion pump involves an applied voltage across a set of cathodes and anodes, which generates electrons that are accelerated toward the anodes. The electrons assume oscillatory and spiral paths due to the magnetic field. The increased path length also increases the probability of collision with gas molecules. The positive ions bombard the cathodes, resulting in the ejection of uncharged cathode atoms that, in turn, eventually bombard the anodes. Chemically active gas atoms, such as O_2 , N_2 and H_2 combine with the reactive atoms and are thus removed, or pumped, from the system.

The situation is different, however, for inert gases such as argon. Once ionized, the molecules either bury themselves in the cathode material, or are reflected and trapped on another surface where sputtering, the act of removing cathode atoms to allow re-emission, is minimal. The pumping speeds are reduced by an order of magnitude, and the pumps try even harder to recover, as shown in Figures 3.11 and 3.12. If it were not for built in safety devices on the linear accelerator ion pumps, the argon poisoning would cause thermal runaway and subsequent damage to the pumps.

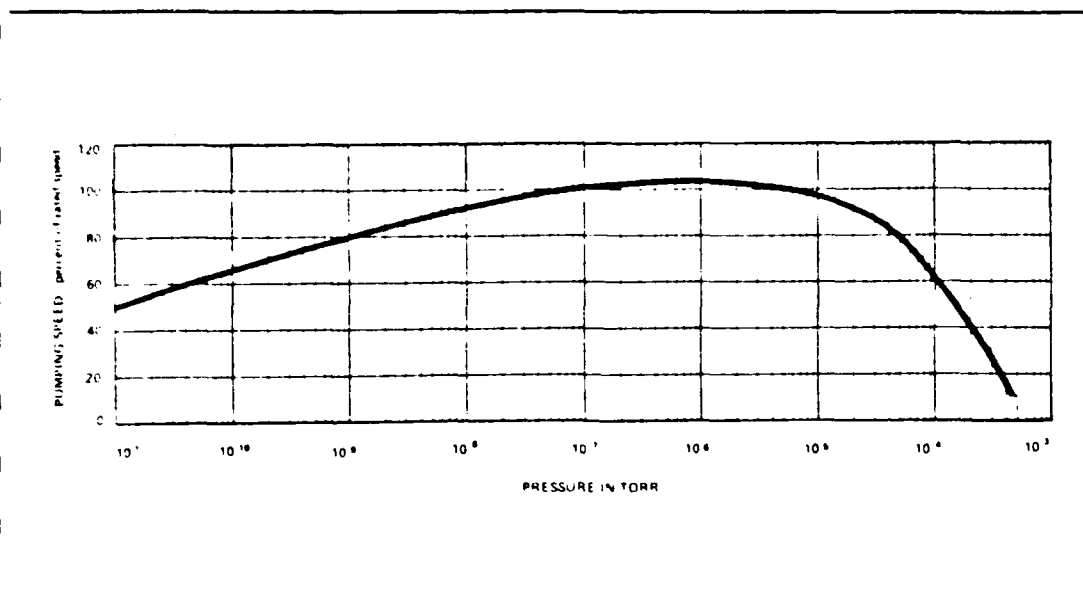


Figure 3.11 Pumping Speed at Various Pressures - Air.

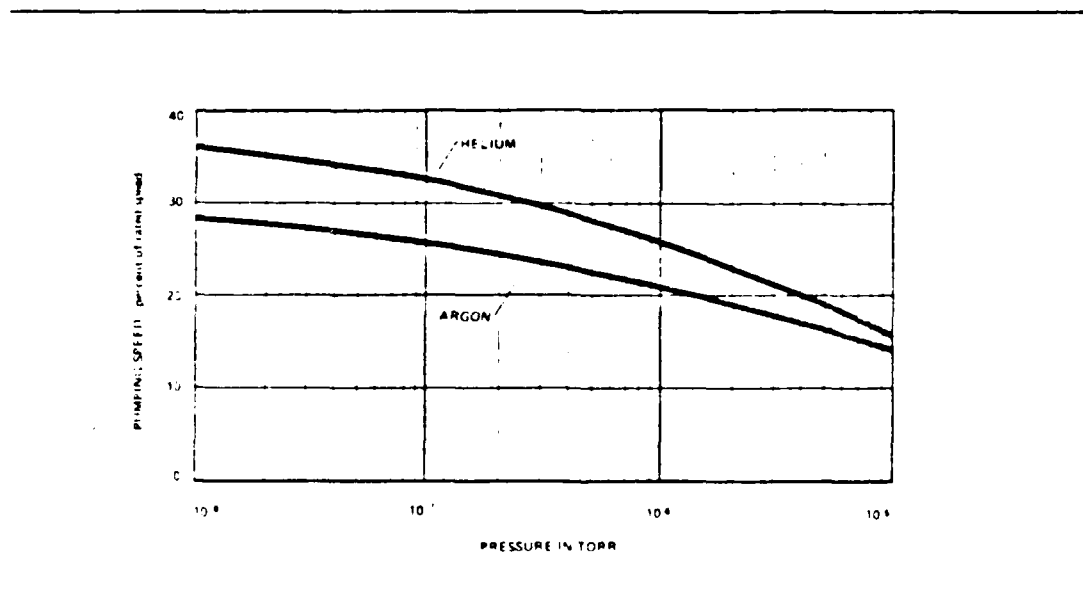


Figure 3.12 Pumping Speed at Various Pressures - Noble Gases.

IV. RESULTS AND DISCUSSION

The electron beam was focused onto the target in the target chamber, and the beam was flattened out in the horizontal direction as it passed through the test chamber and into the beam dump. This could be seen on a coated fluorescent screen material at the beam dump. With the configuration of the aluminum box containing the preamplifier, as shown in Figure 3.1, the edge of the beam struck the detector casing and the preamplifier casing, causing activation of the components and inducing the background radiation observed in Figure 4.1. The radiation level was significantly reduced after waiting a period of two hours, as shown in Figure 4.2. In order to have a reference energy peak, the Fe^{55} source was left in the test chamber, out of the path of the beam and possible Cerenkov radiation. It can be seen in both Figures 4.1 and 4.2.

In order to avoid this interference, the beam was focused on the fluorescent screen located at the exit of the test chamber in the beam dump. At the target, the beam was observed to be flat in the horizontal direction. This beam shape, as opposed to a thin, vertical shape, still allows an accurate determination of the angular displacement of any Cerenkov radiation.

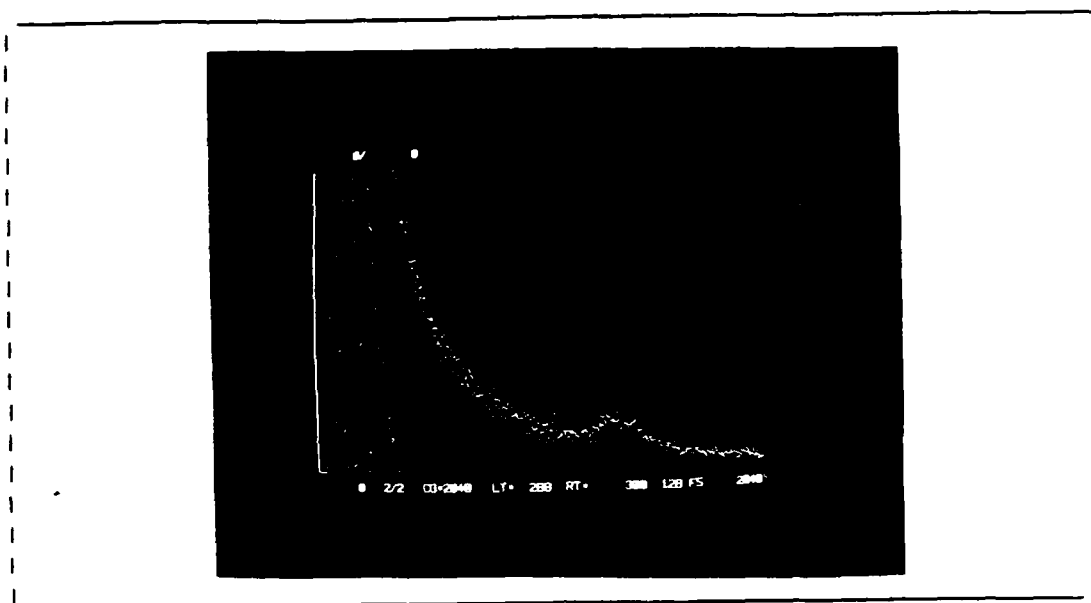


Figure 4.1 PHA Display of Background Radiation.

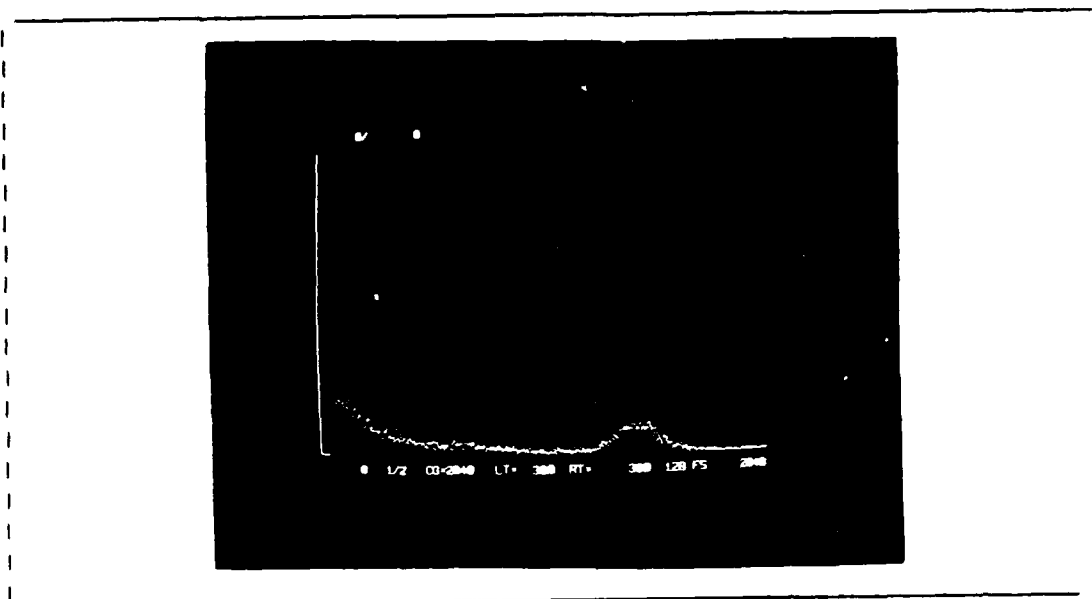


Figure 4.2 PHA Display of Background Radiation after
2 hours.

TABLE C-I

Procedure for the Manufacture of Thin Windows

- 1) Clean shallow pyrex dish with alcohol or acetate, and fill the dish halfway with distilled water.
- 2) Run/skim over surface of water with a paper towel to remove particles.
- 3) Take eye dropper, cleaned in acetate and full of flexible collodion, and dispense a drop on surface of water from a height of at least 12 inches.
- 4) After drop spreads, take wire hoop and place under the surface of the water beneath a spot of film and lift hoop out of water at any small angle, catching the film over the entire area of the wire hoop.
- 5) Let film dry for 10 - 15 minutes.
- 6) While film is drying, cut out section of a thin nylon mesh to place over the 3 x 10 mm window slot
- 7) Take a vacuum sealant and place around slot opening. Ensure slot face is clean.
- 8) Place nylon mesh over opening, and take the window frame assembly and place it on a small container. The diameter of the container must be smaller than the diameter of the wire hoop.
- 9) After film has set for 10-15 minutes, place over window frame assembly and pass the assembly through the hoop. The film will break off the hoop and stick to the vacuum sealant and mesh.
- 10) Let assembly dry for at least four to five hours.
- 11) After the assembly is dry, trim off the excess film. Place vacuum sealant around edges to ensure a good seal and let dry overnight.

APPENDIX C

MANUFACTURING THIN WINDOWS

During a period of time when thin windows were not available or were on order, it was possible to manufacture thin windows with a chemical $C_8H_{11}N$, commonly referred to as Flexible Collodion. Although the amount on hand was rather old, and could only withstand pressures of about 150-180 Torr, the procedure for making them was sound. Table C-I shows the procedure to follow.

gauge maintains a constant reading before leaving the end station area.

In order to return the system back to vacuum, close valve B and secure the gas tank valve. Once pressure meter B returns to 760 Torr, close valve C and valve D, secure Pump 1, and open valve A. It should also be noted that during these procedures, adequate ventilation is required.

C. VENTING THE SYSTEM

In order to bring the system up to atmospheric pressure, extreme care is required to prevent rupture of the thin window. Keeping in mind the need for positive pressure from within the proportional counter to prevent this rupture, close valve A, open the gas vent, and slowly crack open valve B while monitoring pressure meter A. Meanwhile, as the pressure is slowly building in the proportional counter, secure the digital gauge control, and secure the valve to the oil diffusion pump. When the pressure in the proportional counter reaches about 200 Torr, slowly crack open the air vent on the target chamber and monitor the pressure on pressure meter A. Ensuring that the pressure in the proportional counter is always greater than the pressure in the target and test chambers will prevent an unnecessary and costly rupture to the thin window.

TABLE B-I

Valve Alignment for Placing System under Vacuum

Valve A	Open
Valve B	Closed
Valve C	Closed
Valve D	Closed
Gas Vent	Closed
Pump Vent	Closed

at lower vacuum. This reading requires the use of the ion gauge, or gauge no. 2 on the digital gauge control.

B. PRESSURIZING THE PROPORTIONAL COUNTER

Upon reaching the lower limits of the 10^{-5} Torr range, close valve A and thereby isolate the proportional counter from the rest of the system. Ensure both vents are still closed, and then start the mechanical pump for the gas flow system, shown in Figure 3.3 as Pump 1. Open valve D and valve C, which allows the pump to take a suction on the proportional counter lines. Slowly crack open the valve on the gas tank to allow the gas mixture to enter the system up to valve B. Slowly open valve B and monitor pressure meter B. Throttle valve B and valve C to set the correct pressure in the proportional counter. Care should again be exercised here, as the system must be left unattended during the operation of the linear accelerator. Ensure the pressure

APPENDIX B

GENERAL PROCEDURES

A. PLACING THE SYSTEM UNDER VACUUM

Once the test chamber is bolted onto the target chamber, the gas flow system, shown in Figure 3.3, should be aligned as in Table B-I. Once the alignment of valves is completed, the mechanical pump valve should be slowly cracked open. Care should be exercised to ensure that pressure meter A, monitoring the pressure of the target and test chambers, is of a lower pressure, or higher vacuum, than pressure meter B, which monitors the vacuum in the proportional counter. This pressure differential is required to maintain positive pressure on the thin window in the appropriate direction, i.e., in the direction of the mesh support.

When the two meters are reading 760 Torr vacuum, refer to the Perkin Elmer Digital Gauge Control III and monitor gauge no. 1, which should be hooked up to a thermocouple on the inlet to the oil diffusion pump. As gauge no. 1 approaches 100 microns, or 1.0×10^{-1} Torr, shift suction to the oil diffusion pump and secure the mechanical pump valve. The experiment requires a very good vacuum, usually on the order of 2.0×10^{-5} Torr, which may take overnight. The requirement is necessary to prevent high voltage breakdown

APPENDIX A

LIST OF EQUIPMENT

Proportional Counter: Manson Model 04
Choi's Preamplifier [Ref. 6]: Manson Model PAL-01
Preamplifier: EG&G Ortec Model 142 PC
Amplifier: EG&G Ortec Model 450
DC Power Supply: Hewlett Packard Model 6515A
Photomultiplier Tube: RCA Model 6342A
Digital Counters: EG&G Ortec Model 770
Oscilloscope: Tektronix Model 475
Pulse Height Analyzer: Tracor Northern TN-7200
Vacuum Gauge: Perkin Elmer Digital Gauge Control III

x-ray energies may be below the observation limit of the present equipment. Choi has calculated the Cerenkov detection angles for a given thickness of these target materials [Ref. 6]. The problems solved and procedures developed during this experiment will eliminate much of the preliminary benchwork in future experiments.

In addition, consideration should be given to possible improvements of the given experimental apparatus. Addition of another set of quadrupole magnets in the end station could better focus the electron beam, providing an even smaller source of error. Bending the electron beam as it traverses the pipe connecting the target and test chambers, shown in Figure 3.1, with a sufficiently large magnet is another possible modification. This would allow the proportional counter to be lowered all the way to the center position without interfering with the high energy electrons, and thereby eliminate induced radioactivity.

The experiment reported here supports the calculation of Henke et al. [Ref. 3] who predicted an index of refraction less than unity for the K edge of aluminum. No Cerenkov radiation was observed. The previously reported x-ray radiation measurement [Ref. 4] has been shown to be due to sources other than Cerenkov radiation.

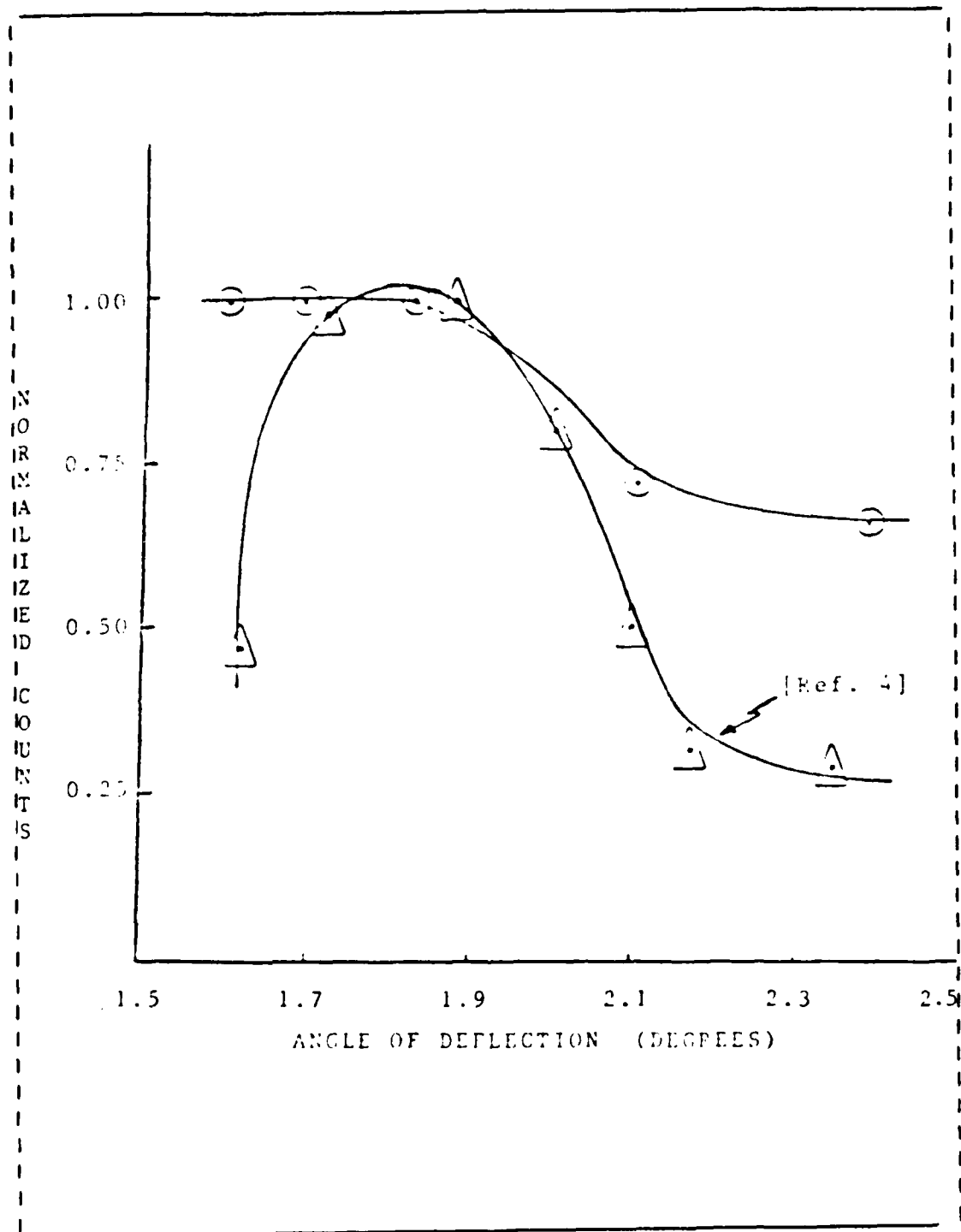


Figure 4.9 Graph of Comparison with [Ref. 4].

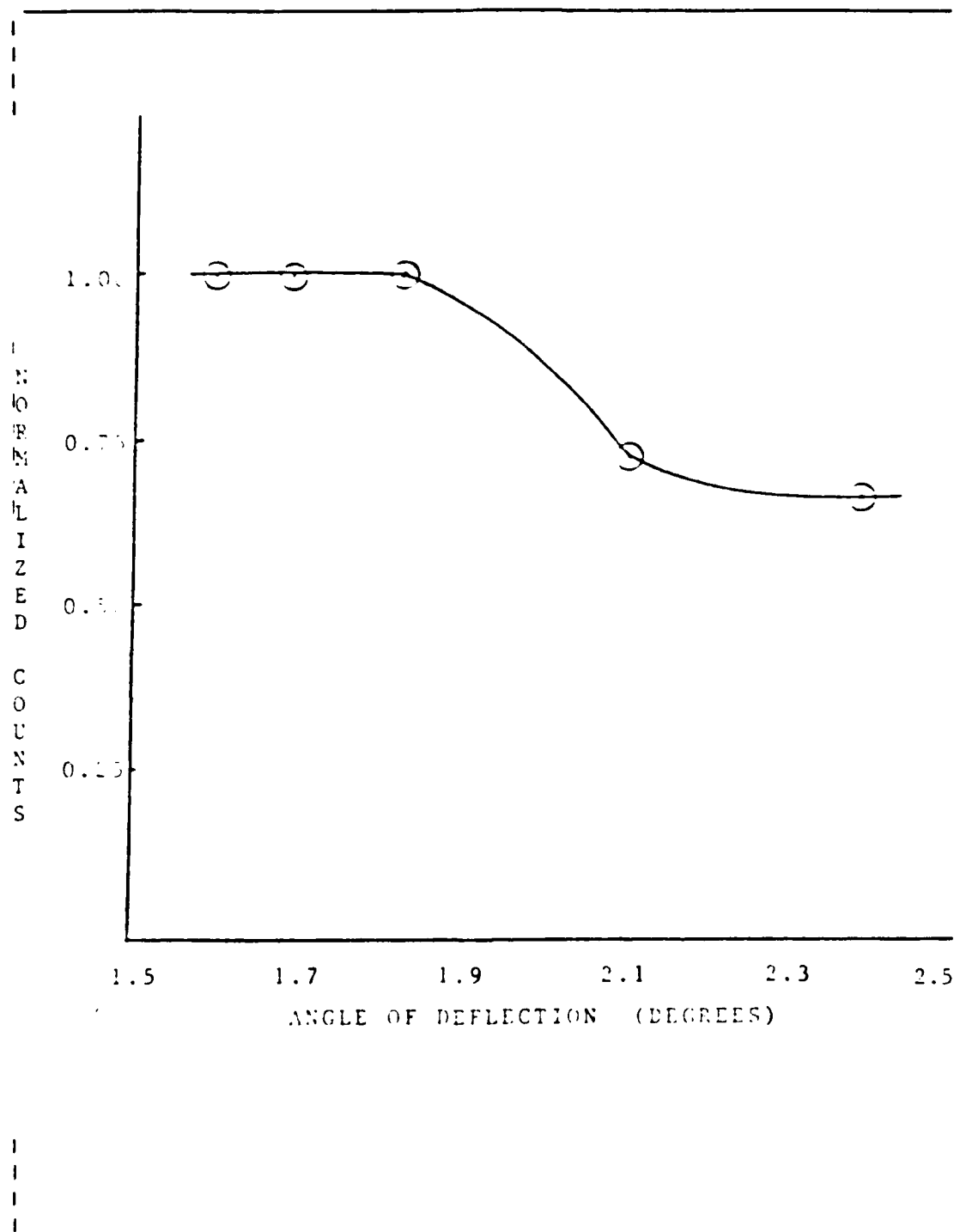


Figure 4.8 Graph of Experimental Results.

Two points must be made here. First, the 1.56 KeV K edge of aluminum was reported by Farmer at 1.58 KeV [Ref. 4]. The peak observed in this experiment was at 954 eV. Second, the peak did not rise sharply in its intensity at a particular angle and sharply drop off as the angle was passed, as is the characteristic of Cerenkov radiation. Figure 4.8 shows a graph of normalized counts versus the deflection angle, θ , in degrees. The curve clearly shows a rise in the number of counts as the angle decreases, but there is no downward trend to establish a peak. Figure 4.9 shows the results of this experiment and Farmer's [Ref. 4] for comparison. It should again be noted that these curves were obtained at different x-ray energies.

With no electrons present, the spectrum showed no counts. This observation ensured that the data taken was due to the electrons and not noise. The spectra obtained when electrons are present is perhaps the result of bremsstrahlung radiation, but most certainly not Cerenkov radiation.

The results obtained during this experiment are consistent with the theory that the index of refraction must be greater than unity in order to obtain Cerenkov radiation. There is more work to be done, however. Future work to further support this theory could include finding the K edge of carbon at 0.28 KeV, the L1 edge of aluminum at 0.87 KeV, and the L2,3 edge of aluminum at 0.73 KeV, though these

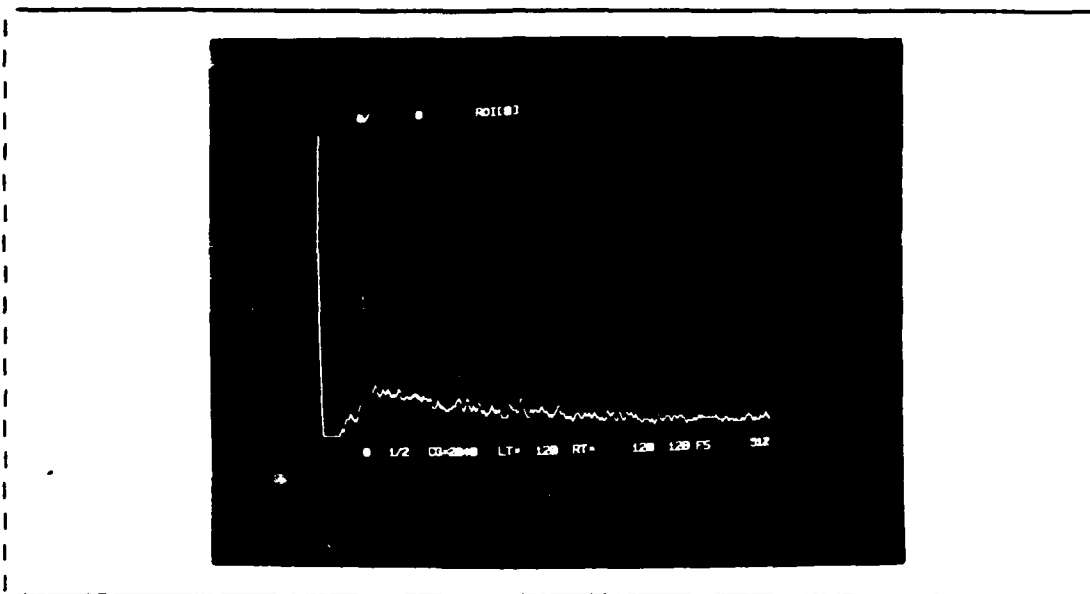


Figure 4.6 PHA Display at 270 Turns (1.828°).

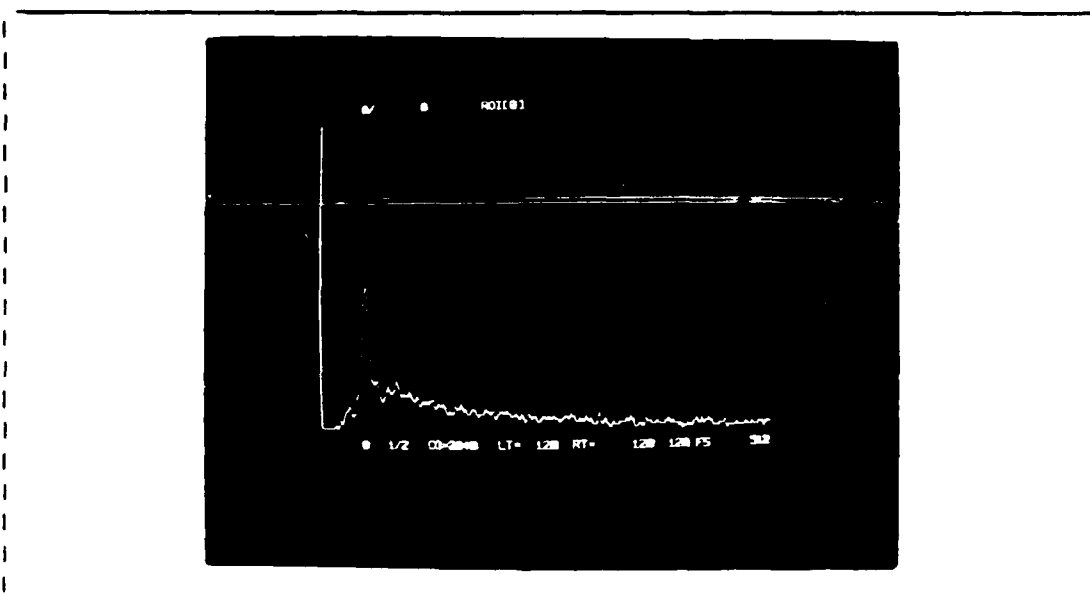


Figure 4.7 PHA Display at 275 Turns (1.690°).

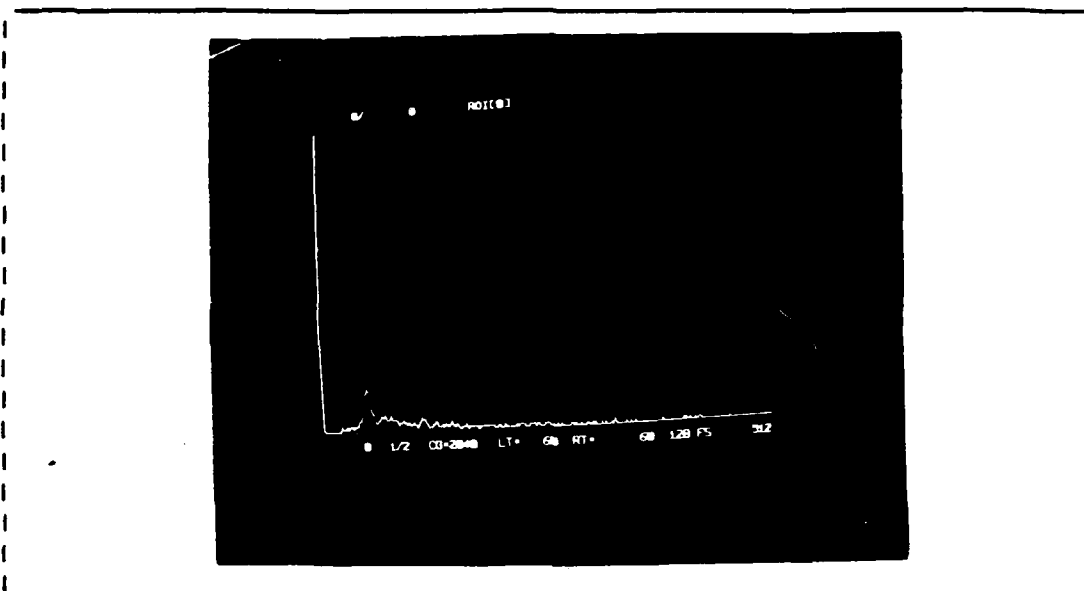


Figure 4.4 PHA Display at 250 Turns (2.382°).

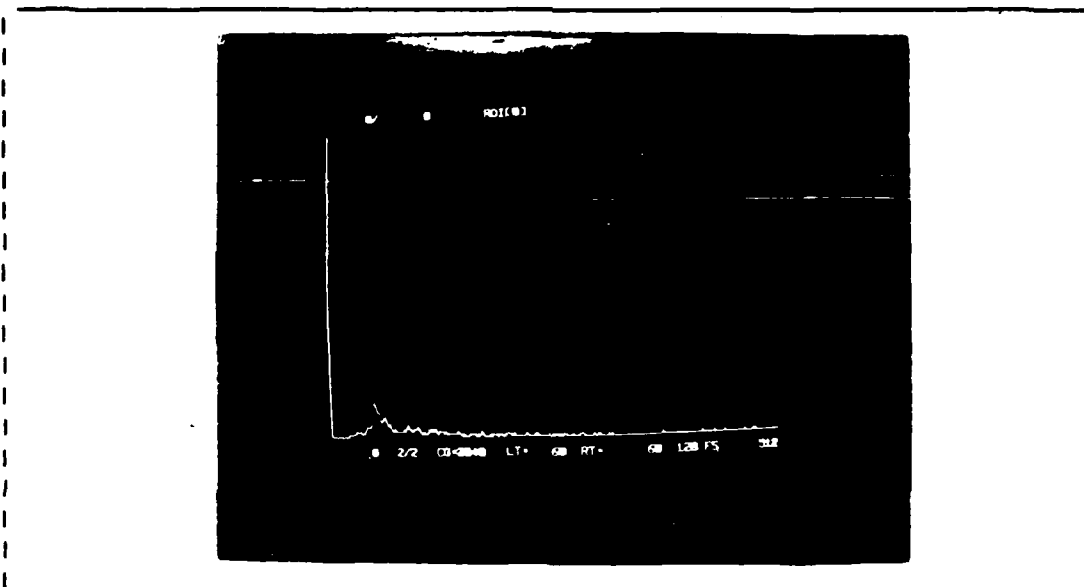


Figure 4.5 PHA Display at 260 Turns (2.105°).

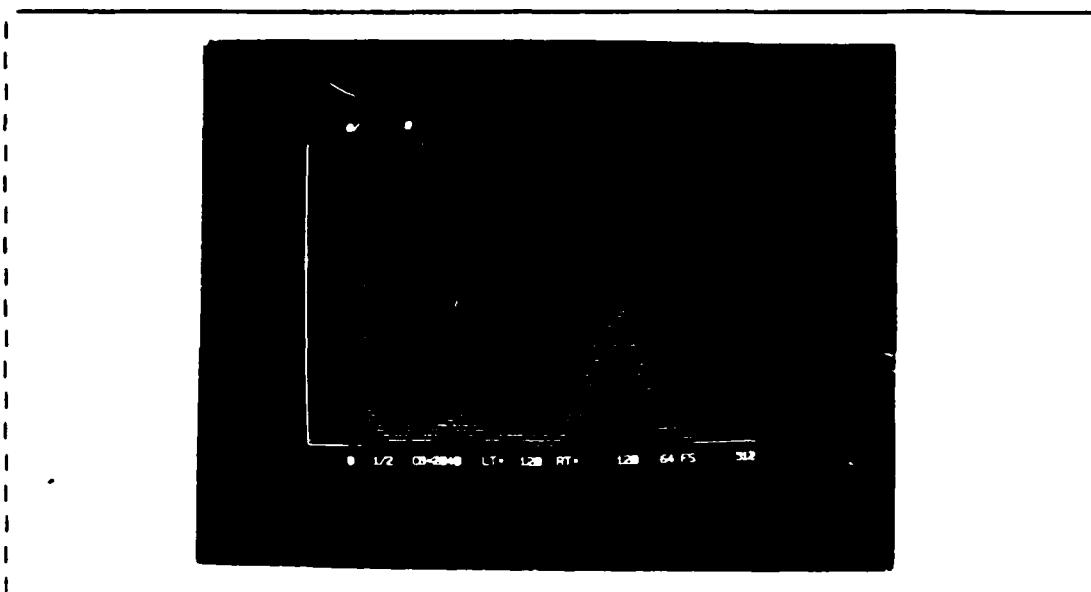


Figure 4.3 PHA Display Showing Klystron Noise.

Figures 4.4, 4.5, 4.6, and 4.7 show the results of the experiment. The lower level discriminator (LLD) on the PHA discriminated out energies below 225 eV. In Figure 4.4, at a turn count of 250 turns, or 2.382° , a peak can be observed at the lower end of the energy spectrum at channel 58. The Fe^{55} source of 5.89 KeV at channel 371, and the Argon K edge of 3.19 KeV at channel 188 are used to calculate an energy of 954 eV at that peak. Figure 4.4 was a 60 second display, as was Figure 4.5 at 260 turns, or 2.105° . Figures 4.6 and 4.7 are 120 second displays showing the peak located at virtually the same channel at 270 and 275 turns, or 1.828° and 1.690° , respectively. The display at 278 (not shown), or 1.607° , was similar to the display at 270 and 275 turns.

With the beam now adjusted, the photomultiplier tube and the plastic scintillation crystal were installed at the exit of the test chamber. The voltage level for the photomultiplier tube was set at 1000 V. This time, however, the electron gun was not used. Stray electrons in the accelerator sections accelerated down the beam pipe at an energy of 95-100 MeV. The x-ray photon rate was reduced to less than one photon per 2-3 machine pulses.

In addition, the PHA display had revealed noise in the lower end of the energy spectrum, as shown in Figure 4.3, and through a series of tests, it was determined that this noise was due to RF from the klystrons. Since low energy peaks could be masked by the klystron noise, a modification had to be made. By gating the PHA, the klystron noise could be removed from the display, thereby allowing low energy peaks to be seen.

The conditions of Farmer's experiment [Ref. 4] were duplicated with the exception of the gas mixture, pressure, and voltage settings. To enhance the lower end of the spectrum, P-50 gas was used at a pressure of 200 Torr, with a voltage setting of 1100 V. Farmer had used P-10 gas at a pressure 250 Torr, and a voltage setting of 920 volts [Ref. 2]. Since these conditions only affect the resolution of the display, and as long as there has been a calibration performed, these differences will not enter into the discussion.

APPENDIX D

MEASUREMENTS AND CALCULATIONS

Figure D.1 shows the dimensions necessary to calculate the maximum angle of clearance for the experiment. From Figure 3.5 the following distances can be calculated:

$$\text{Distance AB} = 60.15 \text{ cm} \quad (\text{D.1})$$

$$\text{Distance BC} = 5.3 \text{ cm} \quad (\text{D.2})$$

$$\text{Total Distance AC} = 65.45 \text{ cm} \quad (\text{D.3})$$

The upper limit that can be achieved with this apparatus places the thin window at 4.8 cm from the top of the chamber. This corresponds to a reading of 100 on the drive motor turn counter. The center position, placing the thin window at 12.3 cm from the top of the chamber, has a corresponding turn count of 336. The maximum angle of clearance is calculated as follows:

$$\tan \theta_1 = (12.3 - 4.8) / 65.45 \quad (\text{D.4})$$

$$\theta_1 = 6.537^\circ \quad (\text{D.5})$$

It should be noted here that point D will not obstruct the maximum angle of 6.537° :

$$\tan \theta_1' = 7.0 / 60.15 \quad (\text{D.6})$$

$$\theta_1' = 6.638^\circ \quad (\text{D.7})$$

$$\theta_1' > \theta_1 \quad (\text{D.8})$$

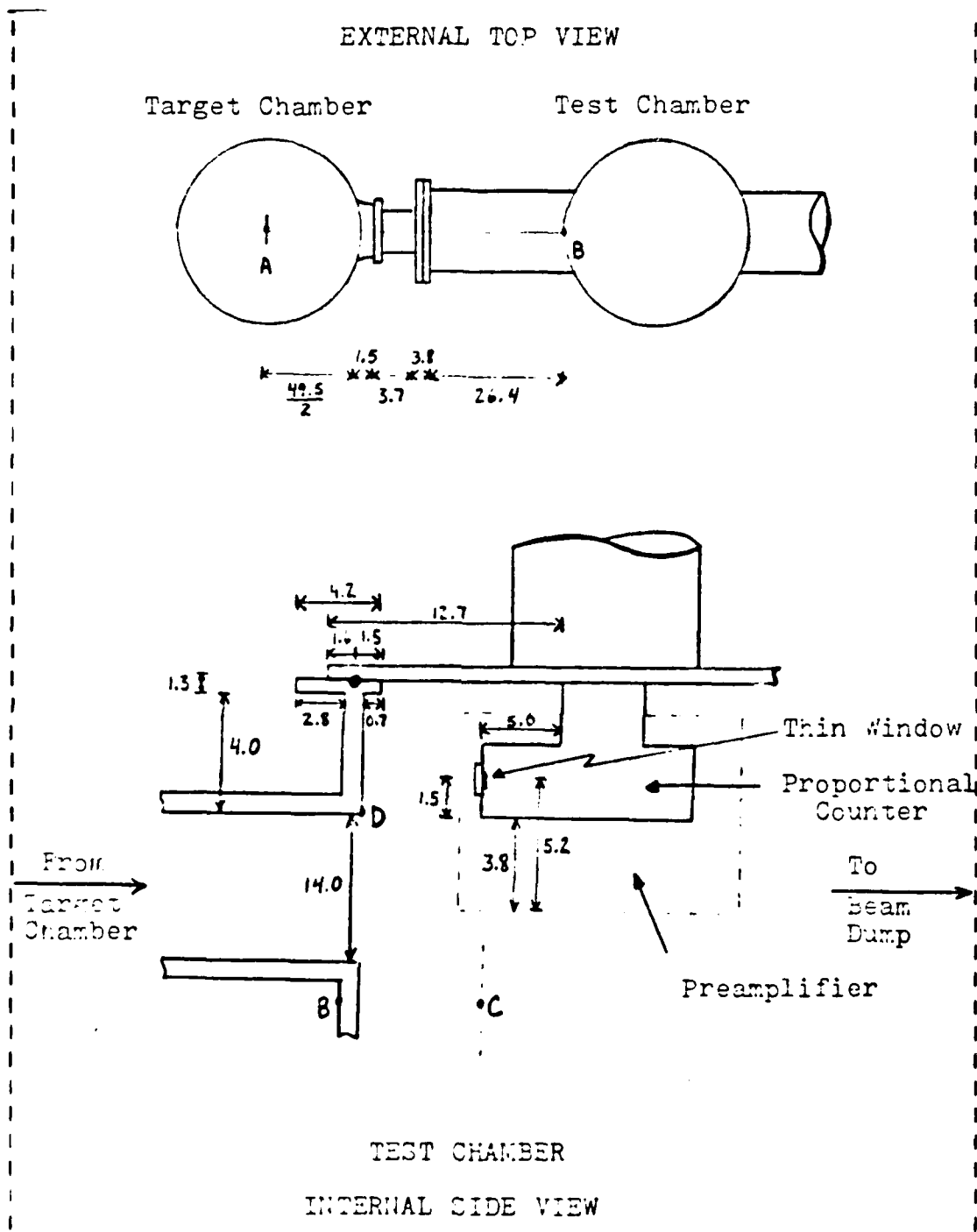


Figure D.1 Test Chamber Dimensions (cm).

In addition, some useful information on the turn count system includes:

$$\text{Angle/Turn} = 0.0277 \text{ deg/turn} \quad (\text{D.9})$$

$$\text{Distance/Turn} = 0.0318 \text{ cm/turn} \quad (\text{D.10})$$

There is another calculation which must be considered in order to pursue the results of Farmer [Ref. 4]. Though the center limit of 336 turns, or 0° is possible, lowering the proportional counter into that region would expose the proportional counter itself to the 100 MeV electrons. Therefore, the minimum angle has to be greater than zero. Looking at Figure 3.5 again, together with a possible beam radius of $1/8$ inch or 0.32 cm, the minimum angle for this experiment can be calculated as follows:

$$\tan \theta_2 = 1.82/65.45 \quad (\text{D.11})$$

$$\theta_2 = 1.593^\circ \quad (\text{D.12})$$

This minimum angle corresponds to 57.23 turns. Since the turn counter is limited in its accuracy, this figure should be set at 58 turns. The turn count lower limit, then, would be 278 turns.

LIST OF REFERENCES

1. Jelley, J. V., Cerenkov Radiation and Its Applications, Pergamon, London, 1958.
2. Bazylev, V. A., et al., "X-ray Cerenkov Radiation. Theory and Experiment," Soviet Physics JETP, v. 45, pp. 224-228, February 1977.
3. Henke, B. L., et al., "Atomic Data and Nuclear Data Tables," Academic Press, v. 27, January 1982.
4. Farmer, W. J., Cerenkov Radiation in the X-ray Region, M. S. Thesis, Naval Postgraduate School, Monterey, California, March 1984.
5. Smith, D. Y., et al., "The Optical Properties and Complex Dielectric Function of Metallic Aluminum from 0.04 to 10 eV," Argonne National Laboratory, March 1983.
6. Choi, Y. D., Design Consideration for the X-ray Cerenkov Experiment, M. S. Thesis, Naval Postgraduate School, Monterey, California, December 1984.
7. Manson, J. E., "The Manson Absolute Photon Counting System for Ultrasoft X-rays," J. E. Manson Co., Inc., Concord, Massachusetts, October 1982.

INITIAL DISTRIBUTION LIST

	No. Copies
1. Library, Code 0142 Naval Postgraduate School Monterey, California 93943-5100	2
2. Physics Library, Code 61 Department of Physics Naval Postgraduate School Monterey, California 93943-5100	2
3. Professor J. R. Neighbours, Code 61Nb Department of Physics Naval Postgraduate School Monterey, California 93943-5100	5
4. Professor X. K. Maruyama B108, Bldg. 245 National Bureau of Standards Gaithersburg, Maryland 20899-5100	5
5. Professor F. R. Buskirk, Code 61Ba Department of Physics Naval Postgraduate School Monterey, California 93943-5100	2
6. Lt. William R. Fritchie, USN c/o Lyle Cox Mailstop L-28 Lawrence Livermore National Laboratory P.O. Box 808 Livermore, California 94550	2
7. Defense Technical Information Center Cameron Station Alexandria, Virginia 22304-6145	2

END

FILMED

11-85

DTIC